Mechanics of Materials 155 (2021) 103774

Contents lists available at ScienceDirect

Mechanics of Materials

journal homepage: www.elsevier.com/locate/mechmat

Negative Poisson's ratio in graphene Miura origami

Fanchao Meng [a], Shuying Chen [a], Wenyan Zhang [a], Pengfei Ou [b], Jing Zhang [c], Cheng Chen [b,d,*], Jun Song [b,**]

[a] Institute for Advanced Studies in Precision Materials, Yantai University, Yantai, Shandong, 264005, China
[b] Department of Mining and Materials Engineering, McGill University, Montréal, Québec, H3A 0C5, Canada
[c] School of Materials Science and Engineering, Northwestern Polytechnical University, Xi'an, Shaanxi, 710072, China
[d] School of Aeronautics, Northwestern Polytechnical University, Xi'an, Shaanxi, 710072, China

ARTICLE INFO

Keywords:
Graphene
Negative Poisson's ratio
Miura origami
Hydrogenation
Modeling and simulation

ABSTRACT

Hydrogenation is a viable approach in transforming two-dimensional (2D) nanosheets into three-dimensional (3D) nanoarchitectures. The present work reported self-folding of 2D graphene into 3D graphene Miura origami assisted by hydrogenation, and studied its Poisson's ratio under external strain using molecular dynamics simulation and continuum modeling. It was found that the graphene Miura origami possesses negative Poisson's ratio, being largely insensitive to the chirality of the folding creases and side lengths of the constituting parallelograms. We further demonstrated the good agreement of Poisson's ratio between the continuum prediction and MD simulation, and identified the origin of their deviation as localized stress concentration at the quad-junction of the graphene Miura origami. The present study provides insights into designing novel 3D nanoarchitectures of programmable functionalities from 2D nanomaterials.

1. Introduction

Graphene, a monolayer of carbon atoms arranged in a two-dimensional (2D) hexagonal lattice (Novoselov et al., 2005), possesses unique and remarkable physical and electronic properties (Wetzel et al., 2015; Berman et al., 2013; Stankovich et al., 2006; Cohen-Tanugi and Grossman, 2012; Doan et al., 2020) that are not available in conventional three-dimensional (3D) materials. The high flexibility of graphene originating from its monoatomic thickness also enables graphene to develop intriguing morphologies beyond its pristine 2D form (Norouzi et al., 2020; Ru et al., 2019; Savin et al., 2019), thus additional functionalities, such as crumpling (Grima et al., 2015) or rippling (Jiang and Park, 2016) induced negative Poisson's ratio, ruga enabled enhancement of fracture toughness (Zhang et al., 2014), corrugation activated modification of the electronic structure and creation of polarized carrier puddles (Deng and Berry, 2016), among others. In particular situations, the exceptional malleability of graphene can allow graphene the ability to spontaneously and controllably transform into novel and complex nanoarchitectures that are beyond the capability of conventional material processing techniques. Some examples include the self-folded carbon nanotube-graphene hybrid to achieve large electronic band gap (Qi et al., 2011), self-folding of graphene into various stable or metastable structures (e.g., sandwiches, knots, rings, etc.) to serve as building blocks of functional nanoarchitectures of unique properties (Patra et al., 2009), and self-assembled graphene nanocage of programmable morphology to reach high-density gas uptake, storage, and release (Zhu and Li, 2014).

One popular method among the various means of amending the morphologies and structures of graphene is chemical functionalization, which alters the hybridization of carbon atoms to achieve morphological and structural changes of graphene (Zhu and Li, 2013, 2014; Yu and Liu, 2007). In particular, hydrogenation of graphene, i.e., bonding atomic hydrogen (H) to the carbon atoms in graphene, changes the hybridization of carbon atoms from sp^2 into sp^3, which results in local structural change around the carbon atoms, and with patterning of H, the local distortion will accumulate to induce spontaneous folding of graphene into desired morphologies. Hydrogenation of graphene has been an approach widely employed in various experiments, e.g., hydrogenation enabled rolling up of graphene nanoribbons to synthesize carbon nanotubes (Yu and Liu, 2007), and it has been demonstrated that hydrogenation can be controllably realized in atomic precision (Sun et al., 2011; Sessi et al., 2009; Zhou and Sun, 2012).

* Corresponding author. School of Aeronautics, Northwestern Polytechnical University, Xi'an, Shaanxi 710072, China.
** Corresponding author. Department of Mining and Materials Engineering, McGill University, Montréal, Québec H3A 0C5, Canada.
E-mail addresses: cheng.chen@nwpu.edu.cn (C. Chen), jun.song2@mcgill.ca (J. Song).

https://doi.org/10.1016/j.mechmat.2021.103774
Received 21 September 2020; Received in revised form 27 December 2020; Accepted 17 January 2021
Available online 21 January 2021

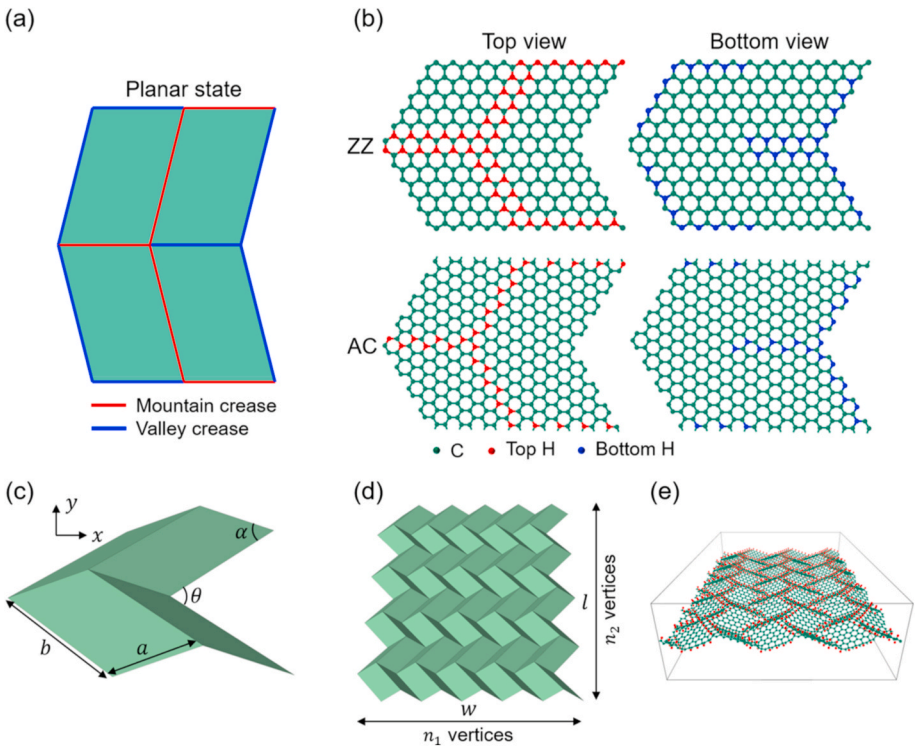

Fig. 1. (a) Schematic illustration and (b) atomic configurations of the graphene Miura origami unit cell in its planar state, where the mountain and valley creases will fold upward and downward, respectively, when folding. The folding in simulations was induced by introducing H to adsorb on top or bottom side of the sheet along the mountain and valley creases, as shown in (b). The Miura origami unit cell after folding is shown in (c), which consists of four identical parallelograms with side lengths of a and b, and an acute angle of α, while θ denotes the projected angle between the two valley creases. (d) Schematic illustration and (e) atomic configuration of a large graphene Miura origami used in simulation, where w and l are length and width of the origami with n_1 and n_2 vertices along x and y directions, respectively. The green and red atoms in (e) respectively indicate C and H atoms. (For interpretation of the references to colour in this figure legend, the reader is referred to the Web version of this article.)

Origami is a class of 3D structures formed by folding 2D sheets along creases, the unique deformability and compactness of which have promised novel functionalities in mechanical (Cromvik and Eriksson, 2006), electronic (Song et al., 2014), and biomedical (Kuribayashi et al., 2006) devices, and it is also an important building block of mechanical metamaterials (Lv et al., 2014). Graphene origami, realized via hydrogenation, has also been reported, and its usage as a high-density hydrogen storage that exceeded the ultimate goal of US Deportment of Energy were demonstrated (Zhu and Li, 2014). Among classes of origami patterns, rigid origami, such as Miura origami, is able to realize folding and unfolding completely through the creases instead of the face bending or partial crumpling, thus possessing important advantages in terms of deformation over most non-rigid origamis (Zheng et al., 2014). In this regard, graphene Miura origami, combining the unique geometrical properties of Miura origami and material properties of graphene, could possess outstanding mechanical and physical properties (Ho et al., 2020a, 2020b). However, to the best of the authors' knowledge, there has been no comprehensive report on the Poisson's ratio behavior of 3D graphene Miura origami under external loading.

Therefore, in this study, we employed molecular dynamics (MD) simulation to simulate the spontaneous folding of graphene sheets of different sizes into nanoscale graphene Miura origamis assisted by selective hydrogenation, and combining continuum modeling, we studied the Poisson's ratio behavior of the graphene Miura origamis under external strain. We found negative Poisson's ratio in graphene Miura origamis and developed continuum model to quantitatively predict the Poisson's ratio that yielded good agreement with MD simulation. In addition, we examined the effects of atomistic arrangement on the Poisson's ratio and identified the deviation between continuum prediction and MD simulation by analyzing the stress state of the graphene Miura origamis.

2. Computational method

The first task in our study is to construct graphene Miura origami structure from a planar graphene sheet via hydrogenation. This was achieved by placing H to adsorb on one or the other side of the sheet along the mountain and valley creases (see Fig. 1a), which subsequently induced spontaneous folding of the planar graphene sheet into graphene Miura origami. Two different groups of graphene origamis were constructed through the above approach, with hydrogenation along either the zigzag (ZZ) or armchair (AC) line, as illustrated in Fig. 1b. In the following, these two groups were denoted as ZZ origami and AC origami, respectively. We note that the amount of H adsorbed along the ZZ or AC line can be varied to modify the folding angle of the graphene Miura origami, i.e., the angle θ between the two valley creases, as illustrated in Fig. 1c (Zhu and Li, 2014). However, we have performed benchmark studies and confirmed that the resultant Poisson's ratio is only dependent on θ, which alternatively can be systematically varied by applying strain (see Section 3 for details). Therefore, representative cases with two columns of H were presented here. As shown in Fig. 1c, after folding, a Miura origami unit cell is comprised by four identical parallelograms, each having side lengths of a and b and an acute angle of α. Note that α always stays constant, being 60° for both ZZ and AC origamis. Large Miura origami sheets are created based on periodic repetition of the unit cell, as demonstrated in Fig. 1d (schematic) and Fig. 1e (simulation). The in-plane dimensions of a Miura origami along x and y directions are denoted as w and l, with the corresponding numbers of vertices being n_1 and n_2, respectively (see Fig. 1d).

Large-scale MD simulations were performed by using the Large-scale Atomic/Molecular Massively Parallel Simulator (LAMMPS) package developed by Sandia National Labs and Temple University (Plimpton, 1995). The interatomic interactions, i.e., carbon-carbon (C–C), C–H and H–H, are described using the adaptive intermolecular reactive empirical bond order (AIREBO) potential (Stuart et al., 2000). The lattice constant of graphene was calculated to be 2.42 Å based on the potential, close to those values reported in previous MD studies on graphene (Meng et al., 2015, 2017). H atoms were introduced at the designated adsorption sites assuming an initial C–H bond length of 1 Å and subsequently the system was equilibrated by performing MD relaxation using the isothermal-isobaric (NPT) ensemble (Hoover, 1985; Nosé, 1984) at a temperature of T = 1 K for a period of 100 ps (ps) to ensure zero stress conditions along all directions. The timestep of 1 fs (fs) was used for all simulations, and periodic boundary conditions (PBCs) were imposed in

Table 1
ZZ and AC graphene Miura origami unit cells of different side lengths (a and b) considered in this study.

ZZ origami	a (Å)	b (Å)	a/b	AC origami	a (Å)	b (Å)	a/b
	29.03	29.03	1		33.52	33.52	1
	38.71	38.71	1		41.90	41.90	1
	48.38	48.38	1		50.28	50.28	1
	38.71	29.03	1.33		41.90	33.52	1.25
	29.03	38.71	0.75		33.52	41.90	0.80
	48.38	29.03	1.67		50.28	33.52	1.50
	29.03	48.38	0.60		33.52	50.28	0.67
	48.38	38.71	1.25		50.28	41.90	1.20
	38.71	48.38	0.80		41.90	50.28	0.83

all directions. The stability (potential energy) and morphology (both atomic configuration and θ) at 300 K of the structure were examined, which yield similar results with those at 1 K. Moreover, the stretching characteristics of the structure are also similar at 1 K and 300 K except that the ultimate tensile stress (UTS) varies (see Supplementary material S1 for details). The simulation supercell was cubic in shape (see Fig. 1e) and contains nine origami unit cells (i.e., 3 × 3 along $x \times y$) of different side lengths of the constituting parallelogram (i.e., a and b, see Fig. 1c and Table 1), where the dimension normal to the graphene sheet was set as 200 Å to avoid interlayer interactions. It is noteworthy that Poisson's ratio of supercells with 5 × 5 and 7 × 7 unit cells were also simulated to examine the dependence of the results on the periodic array of origami unit cells, and we found that the Poisson's ratio of the origami structures is independent of the number of origami unit cells as long as the morphology of the origami structure is retained under external strain. However, the low out-of-plane bending stiffness of pristine graphene makes large-sized graphene Miura origami prone to bend under large applied strains (see Supplementary material S2 for details). The dimensions of the supercell along the x and y axes vary accordingly as the values of a and b change, ranging from 144.98 Å by 159.57 Å to 236.13 Å by 252.52 Å for the ZZ origami, and 169.44 Å by 190.21 Å to 253.99 Å

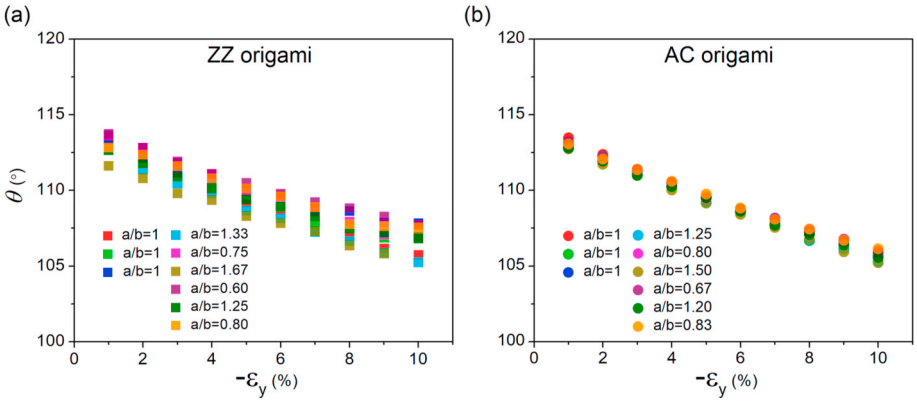

Fig. 2. The projected angle θ between the two valley ridges obtained from MD simulation as a function of applied strain for (a) ZZ and (b) AC origamis of different side length ratios (i.e., a/b).

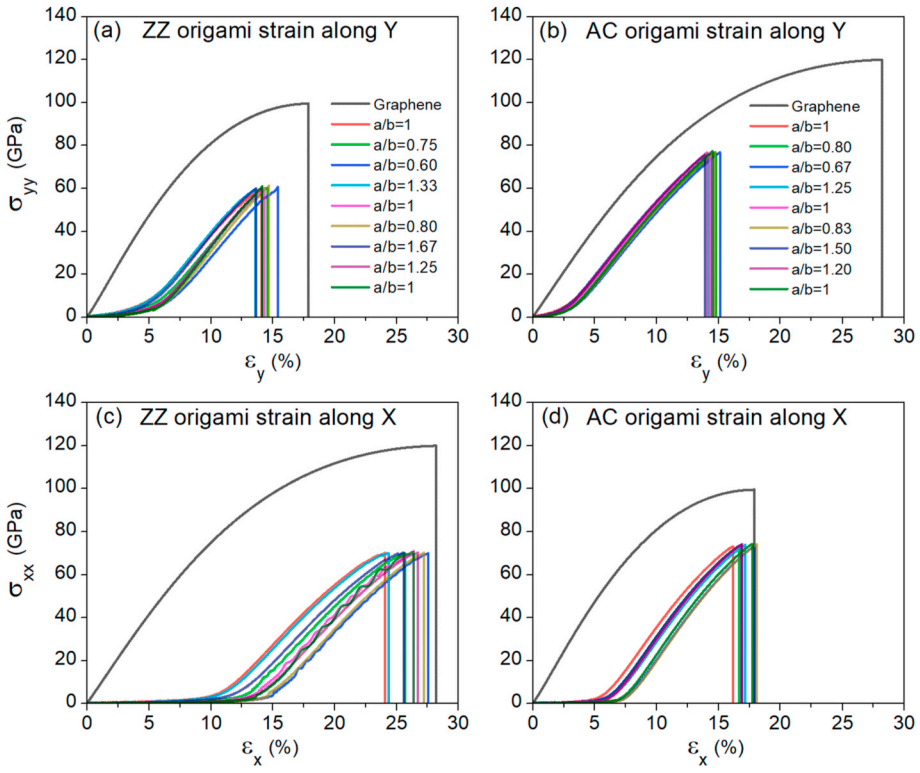

Fig. 3. Uniaxial tensile stress-strain curves for (a) ZZ origamis with strain along y direction, (b) AC origamis with strain along y direction, (c) ZZ origamis with strain along x direction, and (d) AC origamis with strain along x direction, of different side length ratios (i.e., a/b) with comparison with those of pristine graphene. The x and y directions can be referred in Fig. 1c, which correspond to directions normal to the AC and ZZ lines of graphene, respectively, for the ZZ origamis, and vice versa for the AC origamis. The legends of (a) and (b) are applicable to (c) and (d), respectively.

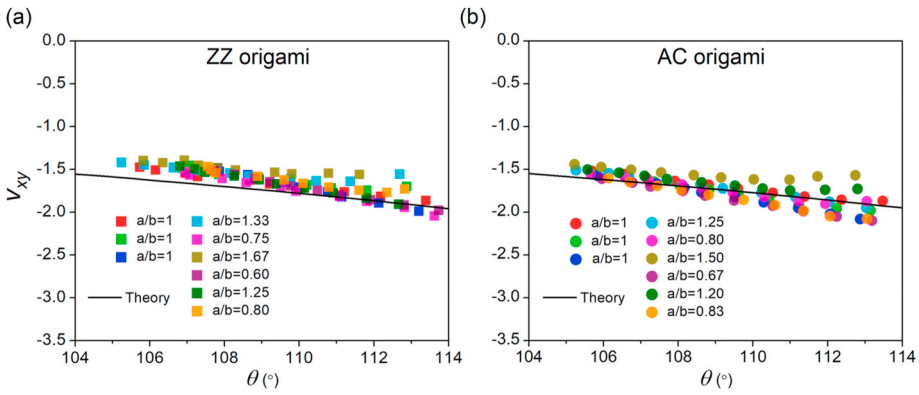

Fig. 4. Poisson's ratio v_{xy} as a function of the projected angle θ between the two valley ridges for (a) ZZ and (b) AC origamis with different side length ratios (i.e., a/b). Symbols and lines are results from simulation and theoretical prediction, respectively.

by 283.71 Å for the AC origami. Benchmark calculations were performed to ensure the simulation results are independent of the size of the simulation cell. After relaxation using the NPT ensemble, the simulation supercell was deformed by a uniaxial compression of a strain rate of 10^{-4} ps^{-1} along the y direction until the desired strain value along y direction, i.e., ε_y, is achieved, up to 10% strain (note that lower strain rates, e.g., 10^{-5} ps^{-1}, have also been tested in additional simulations, yielding negligible difference with the results presented here). This deformation process was also performed in the NPT ensemble, but only maintaining zero-pressure condition for the x direction. After deformation to reach a particular ε_y value, the system was further equilibrated for a duration of 100 ps in NPT, with simulation data from the later 20 ps portion of this duration used to obtain the average supercell dimension along x direction. Subsequently, the strain along x direction, i.e., ε_x, was calculated and the Poisson's ratio $v_{xy} = -\varepsilon_x/\varepsilon_y$ was evaluated. Moreover, similar to the simulation setup of the above uniaxial compression, uniaxial tension along either x or y direction was simulated for both the ZZ and AC origami structures until the structural failure with the C–C bond of the AIREBO potential modified from 1.7 Å to 2.0 Å (Meng et al., 2015, 2017), and the resultant stress-strain response was compared with that of pristine graphene.

3. Results and discussion

When subjected to compressive deformation, the graphene origami structure undergoes changes in its in-plane dimensions and the projected angle θ. Fig. 2 shows plots of the angle θ as a function of the compressive strain along y direction, i.e., -ε_y, for ZZ and AC origamis of different a/b ratios, respectively (note that the change of θ is driven by external strain for a specific a/b ratio). From Fig. 2, we observe θ decreases with the increase of -ε_y, following a similar trend and change of magnitude for both ZZ and AC origamis regardless of the a/b ratios, albeit there is a small variation (~2° in average) among different a/b ratios for the ZZ origami (the origin of such variation will be discussed below). Such an observation indicates that the deformation of the graphene Miura origami is largely insensitive to the chirality of the folding creases and side lengths of the constituting parallelograms.

The results from uniaxial tension for both types of origamis along the x and y directions, respectively (i.e., ZZ origami-strain x, ZZ origami-strain y, AC origami-strain x, and AC origami-strain y, see Fig. 1c of the manuscript for the definition of directions), with comparison with those of pristine graphene, are plotted in Fig. 3. For graphene Miura origami structures, the stress-strain curves of each scenario above are not found to exhibit characteristic differences, except that the failure strain varies among origami structures of different side lengths for each origami type-strain direction pair. Moreover, it is observed that at the beginning of the stretching deformation the origami structure is very soft and a small stress is needed to deform the structure. Particularly for strain long the x direction, stress was not noticeably increased until the strain is beyond 10% and 5% for the ZZ and AC origamis, respectively. Beyond this initial deformation stage, the origami structure becomes stiffened with relatively linear stress-strain response, till the eventual catastrophic brittle failure. The stretchability of origami structures along the x direction is comparable to that of graphene, while that along the y direction is weaker than that of graphene. Furthermore, the UTS of origami structures is less than that of pristine graphene due to the weakening effect of the adsorbed H atoms, which, nevertheless, still retains a very high value being ~70 GPa.

On the basis of Fig. 2, we further plot the Poisson's ratio v_{xy} as a function of the projected angle θ for ZZ and AC graphene Miura origamis of different a/b ratios in Fig. 4. We see that both types of the Miura origami structures have negative Poisson's ratio, consistent with the conclusion of previous study on macroscopic Miura origami structures (Lv et al., 2014; Wei et al., 2013; Schenk and Guest, 2013). Next, v_{xy} of different a/b ratios nearly collapse into one single curve, indicating that Poisson's ratio of graphene Miura origami structure is insensitive to the side length of the constituting parallelogram. Thirdly, v_{xy} is also insensitive to the folding line (i.e., the chirality of the folding creases) of the graphene Miura origami since v_{xy} is nearly the same between ZZ and AC origamis.

To further understand the behavior of the Poisson's ratio of graphene Miura origami, we developed continuum model to quantitatively calculate the Poisson's ratio. v_{xy} is defined as:

$$v_{xy} = -\frac{\varepsilon_x}{\varepsilon_y} = -\frac{(w_\varepsilon - w_0)/w_0}{(l_\varepsilon - l_0)/l_0} \tag{1}$$

where ε_x and ε_y are strains, and w_ε and l_ε and w_0 and l_0 are the dimensions of the simulation supercell (see Fig. 1d) after and before deformation, along the x and y directions, respectively. w_ε and l_ε are defined as:

$$\begin{aligned} w_\varepsilon &= (n_1 - 1)a\cos(\alpha)/\cos(\theta_\varepsilon/2) \\ l_\varepsilon &= (n_2 - 1)b\sin(\theta_\varepsilon/2) \end{aligned} \tag{2}$$

where $n_1 = n_2 = 7$, θ_ε is the projected angle, varying as a function of the applied strain ε_y and was measured based on the output of MD simulation. When $\varepsilon_y = 0$, we have $\theta_\varepsilon = \theta_0$, which is $114.24^\circ \pm 0.4^\circ$ and $114.17^\circ \pm 0.3^\circ$ for ZZ and AC origamis, respectively, calculated from all supercell models with different a/b ratios. Therefore, w_0 and l_0 can be also obtained via Eq. (2). By plugging Eq. (2) into Eq. (1), we obtain:

$$v_{xy} = -\frac{\cos(\theta_0/2)/\cos(\theta_\varepsilon/2) - 1}{\sin(\theta_\varepsilon/2)/\sin(\theta_0/2) - 1} \tag{3}$$

Note that Eq. (3) is independent of the values of a and b, consistent with the observation from the MD simulation. The result of v_{xy} based on Eq. (3) is plotted in Fig. 4, from which we observe that the result from

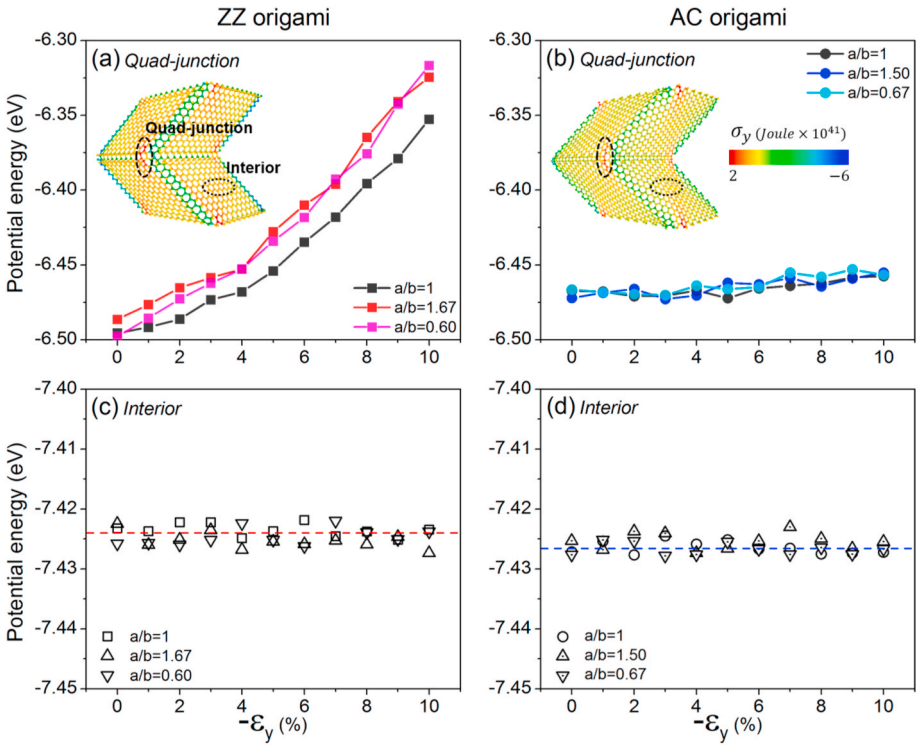

Fig. 5. The evolution of potential energy of the atoms in the quad-junction in (a) and (b) and the atoms in the interior of the constituting parallelogram in (c) and (d) as a function of applied strain for three representative ZZ and AC graphene Miura origamis, respectively. The inset figures in (a) and (b) plot the stress contour along the y direction at −5% strain represented by one unti cell of the Miura origami and ellipses delimit atoms in the quad-junction and the interior.

the continuum model agree relatively well with those from MD simulation.

Although θ (see Fig. 2) and ν_{xy} (see Fig. 4) of both ZZ and AC graphene Miura origamis are largely insensitive to the a/b ratio, we see certain variations of both quantities among structures of different a/b ratios particularly for those of the ZZ origami. In addition, the MD simulated ν_{xy} results of the ZZ origami also exhibits certain offset from those of theoretical prediction especially under large strains. To understand the origin underlying such variation and offset, we examined the configurations of the graphene Miura origami structures with stress contour along the loading direction at a representative strain ($\varepsilon_y = -5\%$) for ZZ and AC origamis, as shown in the inset of Fig. 5a and b. Strong stress concentration was found at the quad-junction formed by the parallelograms for both types of origamis. We further measured the evolution of the potential energy of the atoms within the quad-junction (Fig. 5a and b) and the interior of the parallelogram (Fig. 5c and d) as a function of the applied strain for three representative a/b ratios. It is found that the potential energy of the atoms within the quad-junction (−6.43 eV and −6.46 eV for ZZ and AC origamis, respectively, averaged from the three a/b ratios over the applied range of strain) is apparently higher than that of interior atoms (correspondingly −7.42 eV and −7.43 eV for ZZ and AC origamis, respectively). Therefore, it could be speculated such strong local stress concentration at the quad-junction accounts for the deviation of the MD predicted Poisson's ratio from the theoretical prediction. Moreover, the potential energy of the quad-junction atoms of the ZZ origamis increases more sharply with the increase of the applied strain than that of AC origamis (Fig. 5a), which, on one hand, may account for the variation of θ (Fig. 2a) and stress-strain curves (Fig. 3) among structures of different a/b ratios, and on the other hand, may indicate that the Poisson's ratio of graphene Miura origami can be sensitively dependent on the chirality of the folding creases and the resultant atomic details of the junction after folding. In addition, large-sized graphene Miura origamis are also prone to bend under large applied strains due to the low out-of-plane bending stiffness of pristine graphene (Supplementary material S2), making the Poisson's ratio of graphene Miura origami essentially chirality/junction and size dependent.

4. Conclusions

In summary, we demonstrated hydrogenation assisted self-assembly of nanoscale graphene Miura origami, and studied the evolution of its Poisson's ratio under external strain using MD simulation and continuum modeling. It was found that graphene Miura origami has Negative Poisson's ratio, being largely insensitive to the chirality of the folding creases and the side lengths of the constituting parallelograms. In addition, we derived a continuum model to predict Poisson's ratio of graphene Miura origami, exhibiting good agreement with MD simulation. We further identified stress localization at the quad-junction of the Miura origami as the origin of the deviation between the continuum prediction and MD simulation. Our study offers a viable manufacturing approach to engineer graphene as well as other 2D nanomaterials to achieve 3D nanoarchitectures of novel functionalities.

Authors statement

Fanchao Meng: Conceptualization, Methodology, Simulation, Investigation, Writing. Shuying Chen: Simulation. Wenyan Zhang: Simulation. Pengfei Ou: Methodology. Jing Zhang: Writing. Cheng Chen: Conceptualization, Methodology. Jun Song: Supervision, Writing-Reviewing and Editing.

Declaration of competing interest

The authors declare that they have no known competing financial interests or personal relationships that could have appeared to influence the work reported in this paper.

Acknowledgements

FM and SC acknowledge financial support from National Natural Science Foundation of Guangdong Province-General Program, China (No. 2020A1515011069) and National Natural Science Foundation of China (No. 52001271). JS thanks financial support from Natural Sciences and Engineering Research Council of Canada (NSERC Discovery Grant No. RGPIN-2017-05187). Computing support from Supercomputer Consortium Laval UQAM McGill and Eastern Quebec are greatly recognized.

Appendix A. Supplementary data

Supplementary data to this article can be found online at https://doi.org/10.1016/j.mechmat.2021.103774.

References

Berman, D., Erdemir, A., Sumant, A.V., 2013. Few layer graphene to reduce wear and friction on sliding steel surfaces. Carbon 54, 454–459.
Cohen-Tanugi, D., Grossman, J.C., 2012. Water desalination across nanoporous graphene. Nano Lett. 12 (7), 3602–3608.
Cromvik, C., Eriksson, K., 2006. Airbag folding based on origami mathematics. Origami 4, 129–139.
Deng, S., Berry, V., 2016. Wrinkled, rippled and crumpled graphene: an overview of formation mechanism, electronic properties, and applications. Mater. Today Off. 19 (4), 197–212.
Doan, T., Le-Quang, H., To, Q.-D., 2020. Coupled molecular dynamics and micromechanics study of planar elastic properties of graphene with void defects. Mech. Mater. 103450.
Grima, J.N., Winczewski, S., Mizzi, L., Grech, M.C., Cauchi, R., Gatt, R., Attard, D., Wojciechowski, K.W., Rybicki, J., 2015. Tailoring graphene to achieve negative Poisson's ratio properties. Adv. Mater. 27 (8), 1455–1459.
Ho, D.T., Ho, V.H., Babar, V., Kim, S.Y., Schwingenschlögl, U., 2020a. Complex three-dimensional graphene structures driven by surface functionalization. Nanoscale 12 (18), 10172–10179.
Ho, D.T., Park, H.S., Kim, S.Y., Schwingenschlogl, U., 2020b. Graphene origami with highly tunable coefficient of thermal expansion. ACS Nano 14 (7), 8969–8974.
Hoover, W.G., 1985. Canonical dynamics: equilibrium phase-space distributions. Phys. Rev. A 31 (3), 1695.
Jiang, J.-W., Park, H.S., 2016. Negative Poisson's ratio in single-layer graphene ribbons. Nano Lett. 16 (4), 2657–2662.
Kuribayashi, K., Tsuchiya, K., You, Z., Tomus, D., Umemoto, M., Ito, T., Sasaki, M., 2006. Self-deployable origami stent grafts as a biomedical application of Ni-rich TiNi shape memory alloy foil. Mater. Sci. Eng., A 419 (1–2), 131–137.
Lv, C., Krishnaraju, D., Konjevod, G., Yu, H., Jiang, H., 2014. Origami based mechanical metamaterials. Sci. Rep. 4, 5979.
Meng, F., Chen, C., Song, J., 2015. Dislocation shielding of a nanocrack in graphene: atomistic simulations and continuum modeling. J. Phys. Chem. Lett. 6 (20), 4038–4042.
Meng, F., Chen, C., Song, J., 2017. Lattice trapping and crack decohesion in graphene. Carbon 116, 33–39.
Norouzi, S., Kianfar, A., Fakhrabadi, M.M.S., 2020. Multiscale simulation study of anisotropic nanomechanical properties of graphene spirals and their polymer nanocomposites. Mech. Mater. 103376.
Nosé, S., 1984. A molecular dynamics method for simulations in the canonical ensemble. Mol. Phys. 52 (2), 255–268.
Novoselov, K., Jiang, D., Schedin, F., Booth, T., Khotkevich, V., Morozov, S., Geim, A., 2005. Two-dimensional atomic crystals. Proc. Natl. Acad. Sci. U.S.A. 102 (30), 10451–10453.
Patra, N., Wang, B., Král, P., 2009. Nanodroplet activated and guided folding of graphene nanostructures. Nano Lett. 9 (11), 3766–3771.
Plimpton, S., 1995. Fast parallel algorithms for short-range molecular dynamics. J. Comput. Phys. 117 (1), 1–19.
Qi, J.S., Huang, J.Y., Feng, J., Shi, D.N., Li, J., 2011. The possibility of chemically inert, graphene-based all-carbon electronic devices with 0.8 eV gap. ACS Nano 5 (5), 3475–3482.
Ru, D., Zhu, C., Dong, S., Zhao, J., 2019. Wrinkling behavior of graphene on substrates with different surface morphologies. Mech. Mater. 137, 103144.
Savin, A., Korznikova, E., Dmitriev, S., 2019. Improving bending rigidity of graphene nanoribbons by twisting. Mech. Mater. 137, 103123.
Schenk, M., Guest, S.D., 2013. Geometry of miura-folded metamaterials. Proc. Natl. Acad. Sci. U.S.A. 110 (9), 3276–3281.
Sessi, P., Guest, J.R., Bode, M., Guisinger, N.P., 2009. Patterning graphene at the nanometer scale via hydrogen desorption. Nano Lett. 9 (12), 4343–4347.
Song, Z., Ma, T., Tang, R., Cheng, Q., Wang, X., Krishnaraju, D., Panat, R., Chan, C.K., Yu, H., Jiang, H., 2014. Origami lithium-ion batteries. Nat. Commun. 5 (1), 1–6.
Stankovich, S., Dikin, D.A., Dommett, G.H.B., Kohlhaas, K.M., Zimney, E.J., Stach, E.A., Piner, R.D., Nguyen, S.T., Ruoff, R.S., 2006. Graphene-based composite materials. Nature 442 (7100), 282–286.
Stuart, S.J., Tutein, A.B., Harrison, J.A., 2000. A reactive potential for hydrocarbons with intermolecular interactions. J. Chem. Phys. 112 (14), 6472–6486.
Sun, Z., Pint, C.L., Marcano, D.C., Zhang, C., Yao, J., Ruan, G., Yan, Z., Zhu, Y., Hauge, R. H., Tour, J.M., 2011. Towards hybrid superlattices in graphene. Nat. Commun. 2, 559.
Wei, Z.Y., Guo, Z.V., Dudte, L., Liang, H.Y., Mahadevan, L., 2013. Geometric mechanics of periodic pleated origami. Phys. Rev. Lett. 110 (21), 215501.
Wetzel, E.D., Balu, R., Beaudet, T.D., 2015. A theoretical consideration of the ballistic response of continuous graphene membranes. J. Mech. Phys. Solid. 82, 23–31.
Yu, D., Liu, F., 2007. Synthesis of carbon nanotubes by rolling up patterned graphene nanoribbons using selective atomic adsorption. Nano Lett. 7 (10), 3046–3050.
Zhang, T., Li, X., Gao, H., 2014. Designing graphene structures with controlled distributions of topological defects: a case study of toughness enhancement in graphene ruga. Extrm. Mech. Lett. 1, 3–8.
Zheng, X., Lee, H., Weisgraber, T.H., Shusteff, M., DeOtte, J., Duoss, E.B., Kuntz, J.D., Biener, M.M., Ge, Q., Jackson, J.A., 2014. Ultralight, ultrastiff mechanical metamaterials. Science 344 (6190), 1373–1377.
Zhou, J., Sun, Q., 2012. How to fabricate a semihydrogenated graphene sheet? A promising strategy explored. Appl. Phys. Lett. 101 (7), 073114.
Zhu, S., Li, T., 2013. Hydrogenation enabled scrolling of graphene. J. Phys. D Appl. Phys. 46 (7), 075301.
Zhu, S., Li, T., 2014. Hydrogenation-assisted graphene origami and its application in programmable molecular mass uptake, storage, and release. ACS Nano 8 (3), 2864–2872.